Analysis of Capillary-Driven Viscous Flows During the Sintering of Ceramic Powders

Jorge I. Martínez-Herrera and Jeffrey J. Derby
Dept. of Chemical Engineering and Materials Science, University of Minnesota, Minneapolis, MN 55455

Time-dependent viscous flows driven by capillarity act to minimize the surface area of a fluid bounded in a plane geometry with initial gradients in surface curvature. These free-surface flows are solved by a finite-element model applied to describe the viscous sintering of two-dimensional ceramic particles. The numerical model is validated by comparison to the analytical solution obtained by Hopper (1990) for the coalescence of two infinite cylinders of equal cross section and is applied to several other geometries pertinent to the study of particle sintering for which analytical results are not available. Details of the flow fields and morphological evolution lend insight to the physical behavior of these systems and provide a basis for the more complete understanding of viscous sintering phenomena.

Introduction

A better understanding of fluid dynamical phenomena is often one of the keys to improving technologically important materials processing operations. The theoretical analysis of these systems is made challenging by their complicated geometries and the coupled effects of flow and interfacial phenomena, usually resulting in mathematical free or moving boundary problems (see, for example, Crank, 1984). Some examples of these systems include the growth of large, single crystals (Derby et al., 1985; Cuvelier and Driessen, 1986; Glicksman et al., 1986; Brown, 1988; Derby, 1992), the solidification of molten metals (Szekely, 1988; Viskanta, 1988; Voller, 1991), polymer injection molding (Shen, 1984; Crochet, 1987; Mavridis et al., 1988), and coating flow processes (Kistler and Scriven, 1984; Ruschak, 1985; Benjamin et al., 1991).

An interesting example of the importance of flow in a materials processing system is the sintering of powders of amorphous materials to produce a ceramic component. Under high temperatures, the viscosity of the small particles comprising these materials becomes low enough to flow under the action of surface tension forces. This behavior is known as viscous sintering and is especially important in the production of aerogels and other glassy materials (Rabinovich, 1985; Brinker and Scherer, 1990). Although we focus on viscous sintering in this work, it is important to note that other modes of material transport, primarily diffusional phenomena, may be responsible for the densification of ceramic materials; several excellent general references on sintering can be referred to for more information (Thümmler and Thomma, 1967; Kuczynski, 1972; Kingery et al., 1976; Waldron and Daniell, 1978; Exner, 1979; Yan, 1982; Shaw, 1989a,b,c; Brinker and Scherer, 1990).

Our motivation to better understand the fundamental aspects of viscous sintering arises from a desire to produce improved ceramic materials. Since sintering is frequently the final step in the production of a ceramic material, the density, microstructure, and properties of the material are often profoundly affected by sintering details. These details are influenced by processing conditions, such as the composition of the sintering atmosphere and the heating schedule (Exner, 1979; Yan, 1982; Harmer et al., 1986). A more complete understanding of sintering would aid the optimization of processing conditions to achieve desirable properties of the ceramic material.

Our initial approach to understanding viscous sintering phenomena is the study of rather simple geometrical configurations which are representative of contacting ceramic particles. It is hoped that knowledge gained from these studies will eventually lead to improved constitutive laws describing the densification of macroscopic systems. These laws would be valuable for controlling shape distortion and internal stresses caused by inhomogeneous densification rates which occur during the sintering of large ceramic pieces (see, for example, Evans, 1986).

Frenkel (1945) first analyzed the coalescence of a pair of spheres as representative of the initial sintering of a body of

Correspondence concerning this article should be addressed to J. J. Derby.

packed powder. Frenkel postulated that densification occurred by viscous flow driven by capillarity and suggested that the rate of strain (or densification) could be found by equating the rate of change in the surface energy to the rate of energy dissipation due to flow. Mackenzie and Shuttleworth (1949) put forth similar reasoning to solve for the densification of an amorphous solid with distributed pores to describe the later stages of viscous sintering. Scherer (1977, 1984) also relied on energy balance arguments to solve for the densification of a regular cubic array formed by intersecting liquid cylinders. Scherer's analyses provided reasonable correlations to data obtained from gel densification experiments.

A common weakness of the above analyses involved the assumption of a *specified* sequence of particle geometries for which flows were determined. In reality, the morphology of the system evolves naturally from the initial particle configuration and the driving forces for flow. There have been several efforts to study viscous sintering as a coupled flow and moving boundary problem. Cosgrove et al. (1976) developed an approximate analytical solution for the late stages of the viscous sintering of an array of rods. Ross et al. (1981) employed finite-element methods to describe the viscous sintering of an infinite line of cylinders. Hopper presented exact analytical solutions for various two-dimensional Stokes flows driven by capillarity with free surfaces. The most relevant of these solutions for understanding sintering phenomena are those describing the coalescence of two equal cylinders (Hopper, 1984, 1990) and the disappearance of pores in an infinite continuous medium (Hopper, 1991). Jagota and Dawson (1988, 1990) described the viscous sintering of two initially spherical particles using a finite-element method. Their studies concentrated on the evolving particle geometry and velocity field during the early stages of coalescence and clearly demonstrated the failure of the approach of Frenkel (1945) and others employing geometrical idealizations to quantitatively describe viscous sintering. Kuiken (1990) developed a model for the surface tension driven viscous flow of two-dimensional plane shapes using a boundary element method; however, due to numerical instabilities, only rather smooth shapes could be described. This limitation was remedied later using techniques described by van de Vorst et al. (1992).

We consider two-dimensional viscous flows similar to those studied by Hopper (1984, 1990, 1991), Kuiken (1990), and van de Vorst et al. (1992). Flows of this type are driven by gradients of curvature along a fluid surface. It is the difference in curvature along the surface which produces a spatial distribution of normal forces across the interface. Therefore, any initial geometry with nonconstant surface curvature will lead to time-dependent flows which smooth the surface and minimize the surface perimeter (the surface area is minimized for three-dimensional systems). The long-time equilibrium state of the system is a static fluid contained in a shape whose surface exhibits constant mean curvature. The mathematical formulation of this problem is presented in the next section.

In this study, we employ a finite-element method to calculate numerical solutions to the fundamental equations for capillary-driven flow from arbitrary initial states. This approach sheds considerably more light on viscous sintering phenomena than prior studies which specified an approximate geometrical evolution for the particles. The numerical methods employed here enable the exact morphology of the fluid surface to be calculated self-consistently with the flow field. In addition, this numerical model represents a significant advance over prior models in its ability to handle a wide array of initial configurations efficiently and accurately. Following an outline of our numerical method, we report the flows and geometrical evolution of several two-dimensional initial configurations representative of contacting ceramic particles which subsequently experience viscous sintering. The effects of the initial geometry on the resulting flows and densification rates show the importance of relative surface curvature, initial particle area (volume), and particle connectivity on determining system behavior. These effects are summarized along with some final remarks.

Mathematical Formulation

We consider incompressible, viscous flows driven by capillarity and the accompanying geometrical evolution during the sintering of planar, that is, two-dimensional, particles. We also assume that the flows are isothermal due to the extremely small size of the individual particles. The flows in these configurations are characterized by a fluid density ρ, a fluid viscosity η, a fluid surface tension γ, and a system length scale R_0. A suitable scaling of the Navier-Stokes equation for this problem yields:

$$\frac{\rho\gamma R_0}{\eta^2}\left(\frac{\partial \boldsymbol{v}}{\partial t}+\boldsymbol{v}\cdot\nabla\boldsymbol{v}\right)=\nabla\cdot\boldsymbol{T}+\frac{\rho R_0^2 g}{\gamma}\boldsymbol{e}_g, \tag{1}$$

where $\boldsymbol{v}$ is the dimensionless velocity field, t is the dimensionless time, $\boldsymbol{T}$ is the dimensionless total stress tensor, and $\boldsymbol{e}_g$ is a unit vector oriented with the gravitational vector (g is the gravitational acceleration). Characteristic scales of γ/η for velocity, $\eta R_0/\gamma$ for time, and γ/R_0 for stress are employed to make the above variables dimensionless. The fluid is assumed to be Newtonian, and the dimensionless total stress tensor is defined as:

$$\boldsymbol{T}=-p\boldsymbol{I}+(\nabla\boldsymbol{v}+\nabla\boldsymbol{v}^T),$$

where p is the dimensionless fluid pressure, $\boldsymbol{I}$ is the unit tensor, and T denotes transpose.

The two dimensionless groups in Eq. 1 are defined as the Suratman number Su and the Bond number Bo (Bolz and Tuve, 1973):

$$Su=\frac{\rho\gamma R_0}{\eta^2}=\frac{Re^2}{We}=\frac{Re}{Ca},$$

$$Bo=\frac{\rho R_0^2 g}{\gamma}=\frac{We}{Fr}=\frac{Re\,Ca}{Fr},$$

where Re is the Reynolds number, Ca the capillary number, We is the Weber number, and Fr is the Froude number. Since the characteristic dimension, R_0, is very small in sintering systems, generally on the order of 10^{-5}–10^{-2} cm, and the viscosity, η is very high, often 10^7–10^{10} poise, inertial and gravitational forces are negligible in comparison with both viscous and capillary forces. Characteristic density and surface tension are 1 g/cm^3 and 10^2 dyne/cm, respectively, therefore typical values of the dimensionless groups are $Su=10^{-23}-10^{-14}$ and $Bo=10^{-9}-10^{-3}$. Equation 1 is then reduced to Stoke's equation (in dimensionless form):

$$\nabla \cdot \boldsymbol{T} = \boldsymbol{0}. \tag{2}$$

Specification of continuity completes the field equations describing the flow of this incompressible fluid:

$$\nabla \cdot \boldsymbol{v} = 0. \tag{3}$$

Interestingly, no dimensionless groups are present in the final Eqs. 2 and 3. The physical parameters of a specific system set only the characteristic scales of velocity, time, and stress defined above. Therefore, the only factors which affect the flows in the nondimensionalized problem are geometrical in nature—the initial particle shapes and configuration. This fact allowed Hopper (1990) to construct time-dependent conformal mappings which represented analytical solutions for some specific geometries.

Boundary conditions along the surface of the fluid are provided by a balance of normal and tangential forces at the interface:

$$\boldsymbol{n} \cdot (\boldsymbol{n} \cdot \boldsymbol{T}) + p^* + \kappa = 0, \tag{4}$$

$$\boldsymbol{t} \cdot (\boldsymbol{n} \cdot \boldsymbol{T}) = 0, \tag{5}$$

where $\boldsymbol{n}$ and $\boldsymbol{t}$ are unit vectors normal and tangent to the surface, respectively, p^* is the dimensionless pressure in the gas phase, and κ is the dimensionless mean curvature of the surface (Levich, 1962). Equation 4 represents a balance of normal forces at the interface of the fluid; deviatoric stress components in the gas phase are ignored due to the negligible viscosity of the gas compared to that of the fluid. Gradients of the initial surface curvature lead to differing normal forces along the interface which subsequently drive fluid flow. Equation 5 defines the surface of the fluid to be free of tangential forces and is another consequence of neglecting the deviatoric stress in the gas phase.

Symmetry planes are employed for the geometrical configurations considered here to decrease the size of the computational domain and reduce subsequent calculation costs. Shear stresses along each symmetry plane are set to zero:

$$\boldsymbol{t} \cdot (\boldsymbol{n} \cdot \boldsymbol{T}) = 0, \tag{6}$$

and no flow is permitted across the plane:

$$\boldsymbol{n} \cdot \boldsymbol{v} = 0. \tag{7}$$

These symmetry conditions also serve to implicitly specify a unique solution by fixing the coordinate system with respect to the particles, thus eliminating arbitrary rigid-body translations and rotations from consideration (Kuiken, 1990; van de Vorst et al., 1992).

The fluid interface is a material surface that moves at the same velocity of the contiguous bulk material. This condition is given in dimensionless form by:

$$\boldsymbol{n} \cdot (\boldsymbol{v} - \dot{\boldsymbol{x}}_s) = 0, \quad \text{at} \quad \boldsymbol{x} = \boldsymbol{x}_s, \tag{8}$$

where $\boldsymbol{x}_s$ is the position of the surface and $\dot{\boldsymbol{x}}_s$ is the derivative with respect to time at a fixed parametric position along the interface. If the position of the interface is given by a scalar function $\mathcal{F} = 0$, this kinematic boundary condition (Bird et al., 1960) is expressed as:

$$\frac{\partial \mathcal{F}}{\partial t} + \boldsymbol{v} \cdot \nabla \mathcal{F} = 0. \tag{9}$$

This condition, along with the force balances defined above (Eqs. 4 and 5) completes the specification of the moving boundary of the fluid.

The governing equation set is provided with initial conditions by specification of a boundary shape along with the instantaneous Stoke's flow given by solution of Eqs. 2 and 3 with boundary conditions 4–7 applied on that domain shape. This assures that the initial velocity field is divergence-free. The initial boundary shape can be completely arbitrary; indeed, Hopper (1990, 1991) and Kuiken and co-workers (Kuiken, 1990; van de Vorst et al., 1992) considered many different configurations. However, we consider several initial domain shapes which represent the early contact of two-dimensional particles. This is motivated by our desire to understand the viscous sintering process.

Although we formulate and solve the viscous sintering problem in terms of primitive variables, it is useful also to define the stream function ψ to visualize the flow fields at various times. The stream function is defined in the usual manner for planar flows (Batchelor, 1967):

$$v_x \equiv \frac{\partial \psi}{\partial y}, \quad v_y \equiv -\frac{\partial \psi}{\partial x}.$$

We solve for the stream function by post-processing our velocity field results.

Numerical Methods

Although analytical solutions to this problem exist for certain initial geometries (see Hopper, 1984, 1990, 1991), there are no general methodologies to obtain these solutions. In fact, Hopper (1984) indicates that these solutions have been found by guessing and then verifying parametric forms for the time-evolving domain. We rely instead on numerical method to solve the governing equations for arbitrary initial configurations.

We calculate the moving surface of the fluid with a front tracking method coupled with algebraic mesh generation. This technique has been used with great success to calculate moving boundary problems in a number of different applications (see, for example, Kheshgi and Scriven, 1983; Derby et al., 1987; Ungar et al., 1988). A function is defined to represent the moving surface as follows:

$$\mathcal{F} = r - H(\theta, t) = 0, \tag{10}$$

where r and θ represent the radial and azimuthal coordinates of a cylindrical coordinate system positioned at the center of symmetry of the system and t is the dimensionless time. This representation of the interface, also referred to as a Mongé projection (Ungar et al., 1988), creates a convex quadrangular domain in (r, θ) coordinate space (Figure 1) which facilitates the generation of a finite-element mesh. The mesh consists of quadrilateral elements spaced by a predefined algebraic se-

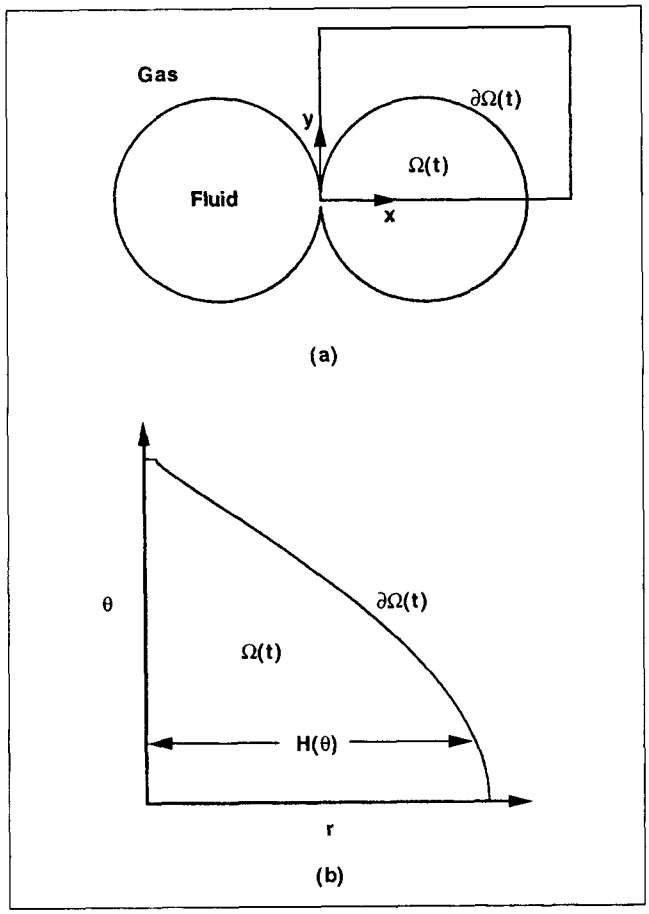

Figure 1. The viscous sintering of planar particles is modeled by flow in a time-evolving fluid domain.

(a) The physical fluid domain is partitioned into a model subdomain using symmetry considerations; (b) the model subdomain is mapped into a computational domain in (r, θ) coordinates, where the fluid surface is readily represented by single-valued function $H(\theta)$.

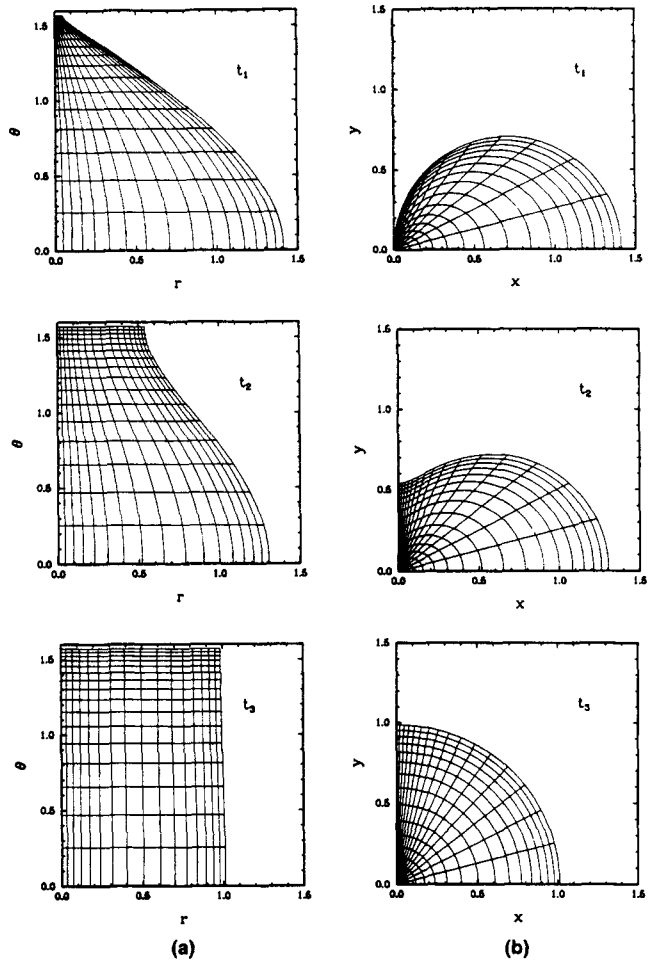

Figure 2. The finite-element mesh evolves in time to track the fluid interface.

(The problem domain is defined in Figure 1.) In these sequences, time increases from the top diagram to the bottom with $t_1 < t_2 < t_3$. (a) The mesh is defined in (r, θ) coordinates in the computational domain; (b) the mesh is mapped to (x, y) coordinates to show the discretization of the physical domain.

quence over the computational domain in (r, θ) space. Since the shape of this domain is defined by the mapping of Eq. 10, the outer edge of the mesh always coincides with the fluid surface, a feature which favors the accurate application of boundary conditions. The mesh thus evolves temporally with the advancing fluid surface; the computational mesh and the corresponding physical domain for the sintering of two equally sized cylindrical particles are shown in Figure 2 (the flows for this case are discussed in the next section).

Based on this mesh, we employ finite-element approximations to the problem unknowns:

$$v_h(r, \theta, t) = \sum_{i=1}^{N} \begin{bmatrix} v_r^i(t)\boldsymbol{e}_r \\ v_\theta^i(t)\boldsymbol{e}_\theta \end{bmatrix} \Phi^i(r, \theta), \tag{11}$$

$$p_h(r, \theta, t) = \sum_{j=1}^{N_p} p^j(t)\Psi^j(r, \theta), \tag{12}$$

$$H_h(\theta, t) = \sum_{\ell=1}^{N_H} H^\ell(t)\Gamma^\ell(\theta), \tag{13}$$

where v_h, p_h, and H_h are the approximations for the velocity, pressure, and surface shape; v_r^i, v_θ^i, p^j, and H^ℓ are the time-dependent unknowns for the spatially discretized problem; $\boldsymbol{e}_r$ and $\boldsymbol{e}_\theta$ are unit coordinate vectors; and N, N_p and N_H are the total number of velocity, pressure, and interface degrees of freedom, respectively. Piecewise continuous and biquadratic Lagrangian basis functions Φ^i are used for interpolating the velocity unknowns, and piecewise discontinuous and linear basis functions Ψ^j are employed for approximating the pressure field. This mixed-order representation was first employed by Engelman et al. (1982) and has proven to be a particularly efficient representation (Gresho, 1985) for solution of the Navier-Stokes equations for incompressible flow. The moving surface is spatially discretized by a piecewise continuous and quadratic Lagrangian basis set Γ^ℓ, which are one-dimensional functions defined along the θ axis.

Galerkin weighted residuals are derived from the governing Eqs. 2, 3, and 9, and the finite-element discretizations of the solution, Eqs. 11-13, are substituted into the resulting integral forms (Strang and Fix, 1972; Dhatt and Touzot, 1984). The residuals for Stoke's Eq. 2 are transformed to the weak form

using the divergence theorem, and the boundary conditions 4-6 are substituted into the resulting surface integrals. A particularly important transformation, first elucidated by Ruschak (1980), allows for the representation of mean surface curvature with first-order derivatives in the weak form of the momentum balance. This significantly facilitates the accurate calculation of surface tension forces at the interface. The no-normal flow condition along the symmetry planes (Eq. 7) is implemented using standard techniques for essential conditions. The resulting Galerkin weighted residual equations are:

$$R_m^i = \int_\Omega T_h : \nabla(\Phi^i e_k) dA + \int_{\partial\Omega} n \cdot T_h \cdot (\Phi^i e_k) ds, \tag{14}$$

$$R_c^j = \int_\Omega \Psi^j (\nabla \cdot v_h) dA, \tag{15}$$

$$R_K^\ell = \int_{\partial\Omega} \Gamma^\ell \left(\frac{\partial \mathcal{F}_h}{\partial t} + v_h \cdot \nabla \mathcal{F}_h \right) ds. \tag{16}$$

The subscript m refers to the momentum balance (Stoke's equations), e_k is a unit vector in the direction $k = r$ and $k = \theta$, h refers to the finite-element approximation to the problem unknowns, and s refers to arc-length along the surface. The domain Ω and the particle surface $\partial\Omega$ are shown in Figure 1. The index i refers to the mesh nodes covering the domain Ω, except those which are associated with the essential conditions of Eq. 7. The subscript c refers to the continuity equation, and index j denotes all finite-element pressure basis functions defined over the mesh (three per element). The subscript K refers to the kinematic condition, and index ℓ represents the number of surface nodes which fall along the interface $\partial\Omega$.

It is convenient and enlightening to represent the mathematical solution of the discretized problem as a vector of time-dependent degrees of freedom (of length $2N + N_p + N_H$) formed by the velocity, pressure, and interface unknowns:

$$y(t) = (\{v_r^i, v_\theta^i, i = 1, \ldots, N\}, \quad \{p^j, j = 1, \ldots, N_p\}, \quad \{H^\ell, \ell = 1, \ldots, N_H\})^T.$$

Then the equation set (Eqs. 14-16) is formally represented by a differential-algebraic equation (Petzold, 1982):

$$M \frac{dy}{dt} = F(y), \tag{17}$$

where the mass matrix M is singular due to the absence of explicit time derivatives in the momentum and continuity equations.

Equation 17 is efficiently solved with a fully implicit, second-order accurate Trapezoid time integration rule. This method yields the following equation to be solved at each time step:

$$\frac{2}{\Delta t} M(y_{n+1} - y_n) - M\dot{y}_n - F_{n+1}(y_{n+1}) = 0, \tag{18}$$

where the subscripts denote the time step, Δt is the time step size, and $\dot{y}_n$ is obtained recursively by inverting the trapezoid rule:

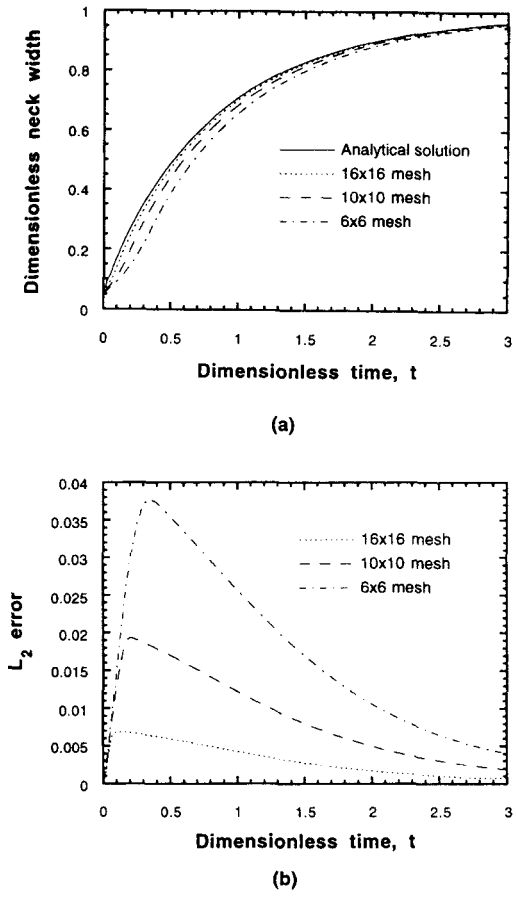

Figure 3. Comparison of finite-element solutions with the analytical solution (Hopper, 1990) for the sintering of two circular particles of equal size demonstrates the convergence of the numerical method.

(a) Comparison of neck width vs. time shows numerical solutions uniformly approaching the analytical solution with finer mesh discretizations; (b) L_2 error of the numerical solutions plotted as a function of time shows errors are greatest at small times. Uniform convergence with mesh is also evident.

$$\dot{y}_n = \frac{2}{\Delta t}(y_n - y_{n-1}) - \dot{y}_{n-1}. \tag{19}$$

The solution of Eq. 18 at each time step is obtained via a Newton-Raphson iterative technique which employs a direct matrix solver. Accurate initial guesses for the iterative method at each time step are provided by a second-order, Adams-Bashforth predictor, which also supplies an error estimate used to control time step size. This strategy was originally described by Gresho et al. (1980); other implementations for moving-boundary problems are described by Derby et al. (1987) and Ungar et al. (1988).

The veracity of the model is corroborated by the results presented in Figure 3, where measures of the numerical solution are compared to the analytical solution obtained by Hopper (1984, 1990) for the viscous sintering of two equally-sized circular particles. The numerical simulations were initiated with a neck width of 7% of the initial particle diameter; the surface shape for this initial condition was obtained from the analytical solution of Hopper. Figure 3a shows neck width vs. time for

the analytical solution and for numerical solutions obtained with three different finite-element meshes. The convergence of the finite-element results to the analytical solution is apparent with increasing spatial discretization, thus demonstrating that the results from the discretized numerical model are numerically convergent to the continuum solution. Note that the time step size employed in Eq. 18 also affects temporal error; however, sufficiently small time steps were used so that the numerical errors were dominated by those arising from the spatial discretizations.

A more quantitative evaluation of the accuracy of the numerical calculations is shown in Figure 3b, where an L_2 error norm defined as:

$$L_2 \text{ error} = \left(\frac{\int_{\partial\Omega} (H_e - H_h)^2 ds}{\int_{\partial\Omega} H_e^2 ds} \right)^{1/2}, \tag{20}$$

is plotted vs. time. In the above definition, H is the radial coordinate of the surface position and is defined by Eq. 10, and the subscripts e and h denote the exact analytical solution and the discretized numerical solution, respectively. This error increases during the initial stages of the sintering, reaches a maximum, and then decreases with time. This behavior is consistent with the severe gradients of curvature which are initially present at the connecting neck region of particle contact. The maximum error in the numerical solutions decreased from approximately 3.8% for the coarse 6×6 mesh to approximately 0.7% for the finest mesh of 16×16 elements (shown in Figure 2).

All subsequent calculations reported here employ a mesh comparable to the fine mesh of 16×16 elements used for the two equally-sized particle simulation. This specific mesh consisted of 256 elements with a total of 2,979 mathematical unknowns. The computation of this case (starting from an initial neck width of 7% of initial particle size to a final neck width of 99% of the final single particle diameter, corresponding to a dimensionless time of $t \approx 4$) was typical of all calculations considered and required approximately 30 CPU min on the Cray X-MP of the Minnesota Supercomputer Center.

Results

In the following sections, several initial configurations which are representative of the sintering of two-dimensional particles are considered. All calculations begin at time zero with a small but finite neck whose width is set at 7% of the size of the larger particles of the initial configuration. This value was chosen as a reasonable compromise between the representation of neck formation at very short times and the rather significant computational resources required for their accurate calculation. The simulation of particle evolution from smaller initial neck widths is feasible but requires much finer meshes with concomitant increases in computation time (Martínez-Herrera, 1994).

The initial surface shapes are provided from the analytical solution of Hopper (1984, 1990) for the neck size employed to start the computation. For the simulations of unequal particle size, the initial surface shape is constructed by matching each half of two different Hopper solutions at their planes of symmetry: the shape of the larger particle is that obtained from one half of the analytical solution for two equal particles sintering with a neck size of 7% of the initial particle diameter, while the profile of the smaller particle is taken from the analytical solution for two identical small particles at a larger relative neck size. Matching the two different particle profiles is made possible by the common zero-slope condition on the surface shape across the centerline for the analytical solutions.

The large gradient of interface curvature associated with the small initial neck drives flows which promote growth of the neck region. Flow continues until an equilibrium shape with constant mean curvature everywhere is attained. The initial system size and geometry greatly affect the rate at which this equilibrium state is approached, as seen in the following simulations.

Two circular particles of equal size

We first study the viscous sintering of two infinite cylinders of equal size. This case has been solved analytically by Hopper (1984, 1990); however, the details of the flow field were not explicitly presented by Hopper, rather only the geometrical evolution of the surface was shown. Our solution for this particular case serves dual roles; it provides a benchmark to assess the accuracy of our numerical method, and it also serves as the simplest case relevant for the study of the flows during the viscous sintering of particles.

Figure 4 shows the geometrical evolution and flow streamlines for the sintering of two circular particles, each of initial dimensionless radius $1/\sqrt{2}$. Initially, the interface curvature is positive everywhere except in the neck region where the particles make contact, hence the normal surface traction is negative everywhere except at the neck surface, where it is positive and provides the driving force for the deformation. The domain changes rapidly during the first stages of sintering with material flowing from the outer lobes toward the neck region. Interestingly, even though the driving forces arise at the fluid interface, this flow occurs throughout the bulk of the particle rather than along the particle surface. Eventually, the two particles coalesce into a larger single particle with a radius of unity in the limit of time approaching infinity.

The maximum value of the stream function is plotted as a function of time in Figure 5 and indicates that the total flux of fluid volume associated with this flow increases to a maximum at $t \approx 0.5$ and then slowly decreases. The driving forces for flow are greatest with the large curvature of the neck region at time zero. However, the small initial neck encloses only a relatively small amount of fluid, and the overall flow of material continues to increase as the neck enlarges. Eventually, the growth of the neck reduces the gradients of surface curvature and the driving force for flow subsides. The negative curvature of the neck region disappears at $t \approx 1.1$ (see Figure 4) and the geometrical evolution of the surface slows significantly. Differences in mean curvature around the surface continue to drive a weak flow until the curvature is everywhere constant and a perfect circular shape is attained.

Two circular particles of different size

Next, we consider the sintering of two circular particles of unequal size. Unlike the previous problem of two identical particles, a purely analytical solution for this initial geometry is not known. Also, this problem possesses only one axis of symmetry along the line connecting the centers of the two

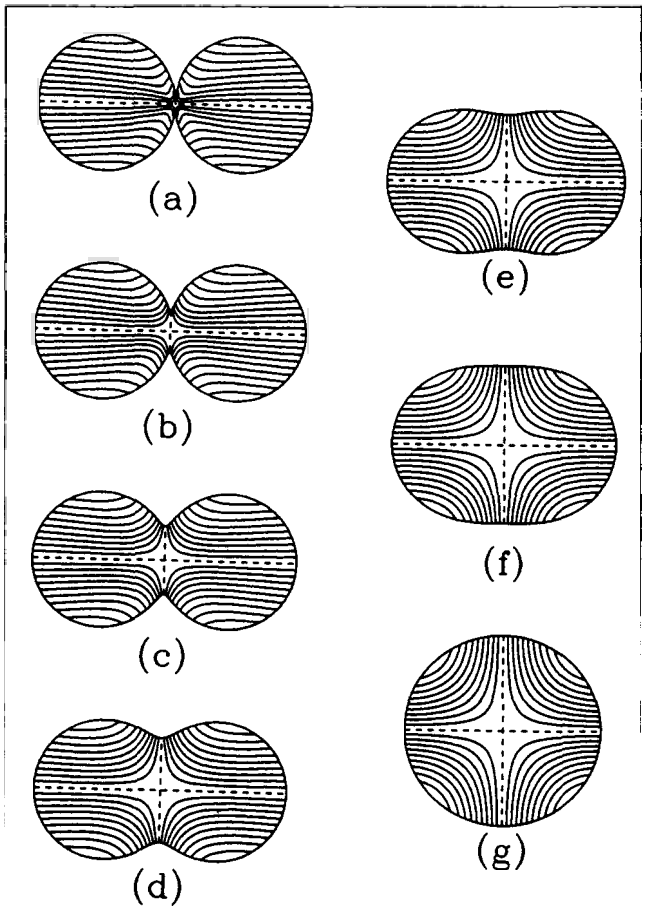

Figure 4. Evolving particle shape is shown along with instantaneous stream function contours for the sintering of two circular particles of equal size.

10 streamlines are plotted with equal spacing between zero and the maximum absolute value of ψ. The zero stream function is defined along symmetry planes and is indicated by dashed lines. The sign of the stream function alternates between adjacent quadrants. For the indicated geometries: (a) $t=0$; (b) $t=0.164$; (c) $t=0.333$; (d) $t=0.618$; (e) $t=1.002$; (f) $t=1.146$; (g) $t=4.062$.

particles, therefore a larger computational domain (consisting of 16×32 elements) covering half of the system rather than a quadrant is employed.

Figure 6 shows the evolution of shape and instantaneous streamlines for a small particle of radius $1/4\sqrt{2}$ initially contacted with a larger particle of radius $1/\sqrt{2}$. For this initial configuration, the neck region is rapidly filled, followed by a slower smoothing of the protrusion caused by the smaller particle until the equilibrium circular state is achieved. Interestingly, the near-equilibrium state of Figure 6g shows that the final distribution of the material originally contained by the smaller particle is very localized.

As in the identical particle geometry considered above, the flows occur through the bulk of both particles as material moves from the outer lobes to the neck region. The stream function maximum increases to a peak value at $t\approx0.2$ and then decreases (see Figure 5). Although the causes of this behavior are the same as discussed in the previous section, the stream function maximum is larger and occurs at a shorter

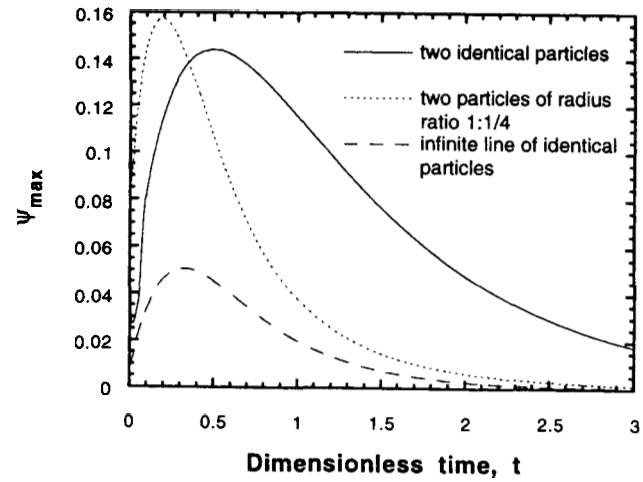

Figure 5. The maximum stream function value plotted as a function of time shows that the overall flow increases initially and then decreases with time for all initial geometries considered here.

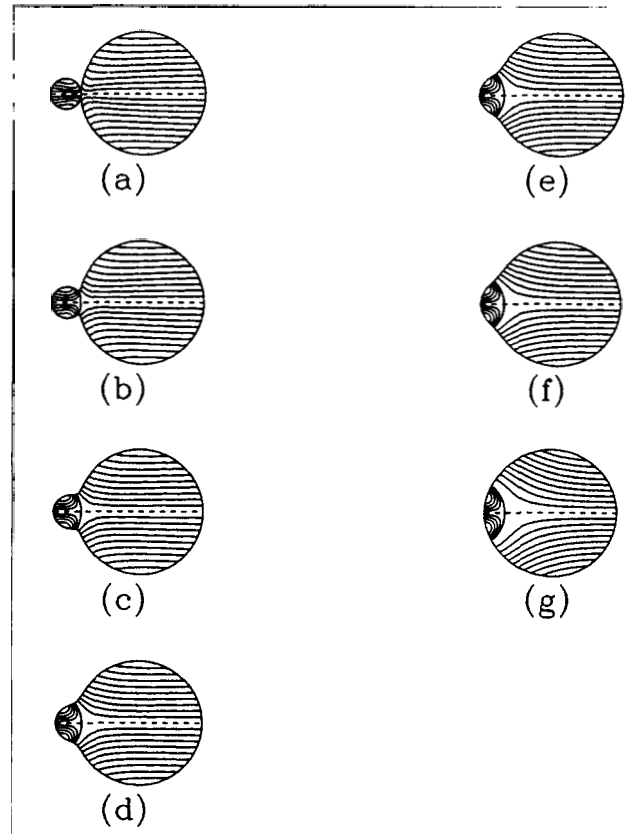

Figure 6. Evolving particle shape is shown along with instantaneous stream function contours for the sintering of two circular particles whose initial ratio of particle radii is 1:1/4.

10 streamlines are plotted with equal spacing between zero and the maximum absolute value of ψ for the larger particle; 5 equally-spaced streamlines are plotted for the smaller particle. The zero stream function is defined along the symmetry plane (dashed line) and the plane of initial contact (solid line). The sign of the stream function alternates between adjacent quadrants. For the indicated geometries: (a) $t=0$; (b) $t=0.095$; (c) $t=0.200$; (d) $t=0.297$; (e) $t=0.372$; (f) $t=0.494$; (g) $t=1.172$.

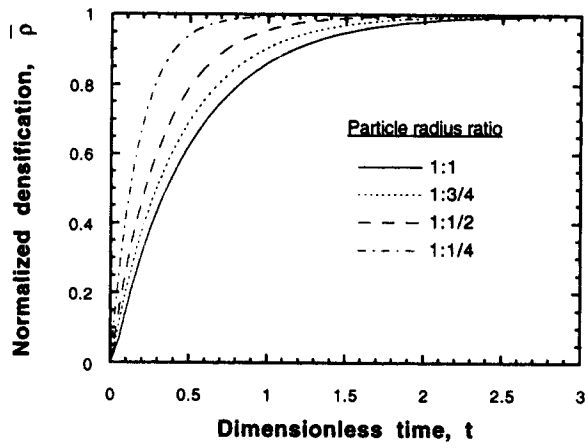

(a)

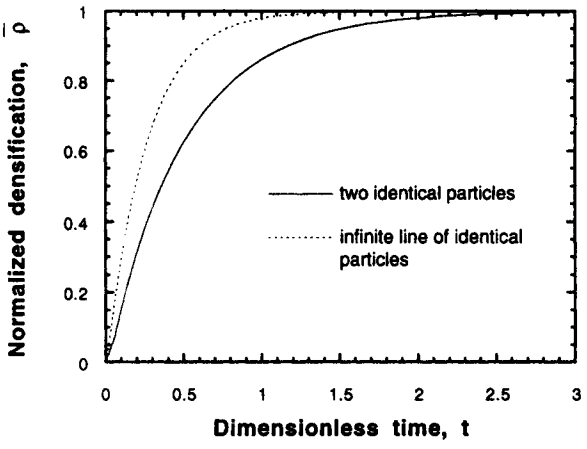

(b)

Figure 7. The rate of densification, $\bar{\rho}$ (defined in text), depends on system size, shape, and topology.

(a) Two-particle systems densify faster with one smaller particle because of increasing mean surface curvature and decreasing total volume. These effects are more pronounced with decreasing diameter of the smaller particle; (b) an infinite line of equally-sized particles densifies faster than two identical particles because of the increased number of contact points per particle.

time than in the case of two equal-sized particles. This is explained by the greater driving forces for flow which arise from the higher mean curvature of the neck between the smaller and larger particle.

An important characteristic of the macroscopic sintering of a powder compact is the rate at which densification occurs. A representative measure of densification for the simple geometries considered here is the extent of coalescence of the initial particles to the equilibrium configuration. We define a normalized measure of densification, $\bar{\rho}$, as follows:

$$\bar{\rho} \equiv \frac{S_0 - S(t)}{S_0 - S_\infty}, \tag{21}$$

where S is the total surface area of the system (the total arc length for the two-dimensional system considered here), and

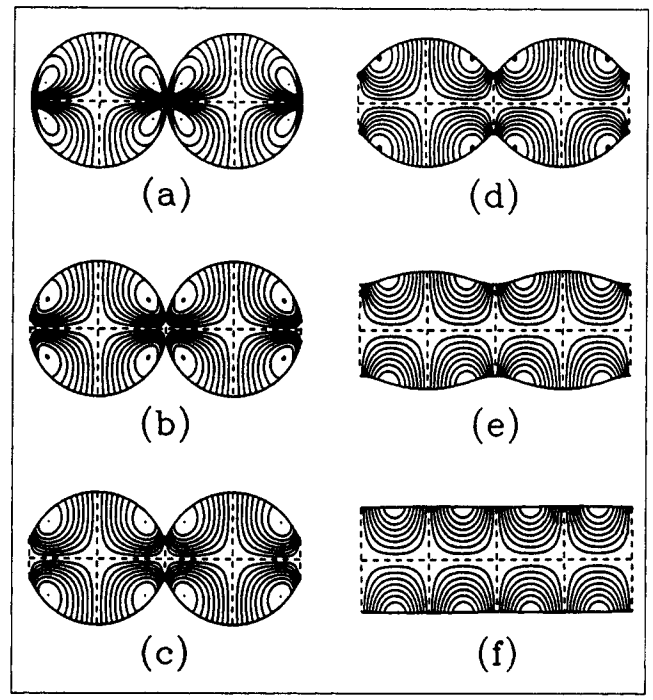

Figure 8. Evolving particle shape is shown along with instantaneous stream function contours for the sintering of an infinite line of identical circular particles (two particles from the configuration are shown).

Nine streamlines are plotted per initial particle quadrant with equal spacing between zero and the maximum absolute value of ψ. The zero stream function is defined along symmetry planes and is indicated by dashed lines. The sign of the stream function alternates between adjacent quadrants. For the indicated geometries: (a) $t=0$; (b) $t=0.084$; (c) $t=0.173$; (d) $t=0.312$; (e) $t=0.781$; (f) $t=2.219$.

the subscripts 0 and ∞ refer to the initial and equilibrium configurations, respectively. Figure 7a shows this quantity plotted vs. dimensionless time (scaled with the uniform radius of the larger particle) for various two-particle configurations. The rate of densification is greater and the time needed to achieve full densification, that is, the equilibrium shape, is shorter as the size of the smaller particle is decreased. This effect is due to two effects which depend on the length scale of the smaller particle. As mentioned above, a smaller particle will result in a larger initial curvature at the neck between the two particles, thus generating a stronger driving force for flow. Also, less material is enclosed by a smaller particle, so that the total flow needed to attain the equilibrium shape is reduced.

Infinite line of circular particles

Finally, the sintering of a system consisting of an infinite line of identical circular particles is studied. The initial radius of each particle is set at $1/\sqrt{2}$, identical to the size employed for the two-particle case. There are three planes of symmetry for this configuration, so the computational domain consisted of only one-quarter of a single particle.

Figure 8 shows the evolution of the system morphology and the instantaneous stream functions for two particles of the infinite chain. The domain changes rapidly during the first stages of sintering and eventually relaxes to the equilibrium

shape of an infinite planar slab. The streamlines indicate that material flows from the upper and lower portions of the particles into the neck area. However, these flows are quite different from those for the two-particle systems considered previously. There is a significant turning of the flow at the particle centers caused by the increased symmetry of the system. In addition, small recirculation cells are exhibited by the flow at early times.

Similar to the flows of the prior configurations, the maximum stream function value increases to a maximum (at $t \approx 0.3$) and then decreases with time (see Figure 5). The maximum is reached at an earlier time than that for the case of two identical particles. Figure 7b shows the densification behavior for this system compared to the two-particle configuration. The faster increase in flow intensity and the more rapid densification occur because there are two contacts (necks) per particle for the infinite line of cylinders. Each initial contact drives a flow, and the resulting flows are confined to smaller spatial regions due to symmetry. Thus, the net flow of material needed to reach the equilibrium shape is reduced compared to the two-particle geometry. However, it should be noted that this configuration is a somewhat idealized representation of any finite chain of particles, since the infinite chain considered here is constrained against shortening.

Summary and Discussion

A finite-element method has been developed to successfully solve for viscous plane flows driven by capillarity, and this method has been applied to study the viscous sintering of two-dimensional particles. The methodology was validated by comparison with the analytical solution available for the coalescence of two equally sized finite cylinders (Hopper, 1984, 1990). This approach allows for the study of arbitrary initial geometries and is significantly more efficient than many prior numerical implementations (Martínez-Herrera, 1994). However, it should be stressed that the sintering of real particles is an inherently three-dimensional phenomenon and that the two-dimensional results presented here provide only qualitative insights to this process.

The flows of these systems are driven by gradients of curvature leading to inhomogeneous *normal* forces along the particle interfaces. Accordingly, these flows are not confined to the surfaces of the particles but occur predominantly through the bulk of the particle, transporting material toward the growing neck. All flows show the global character of increasing in intensity with time to a maximum followed by a subsiding of the flow as the particles relax to their equilibrium configurations. The specific form of these flows is important in real systems, especially with regard to the possible mixing of particles of differing composition. For example, the original material of a small particle sintering to a large particle is very localized in the final equilibrium configuration (see Figure 6). This result would have important implications for the mixing of particles of different composition during viscous sintering (of course, diffusion would also affect the intermixing of material).

The rate at which these systems densify to their equilibrium configuration is also illustrative of the behavior of sintering systems. In general, systems with smaller length scales, that is, smaller particles, approach their equilibrium configurations much more quickly. This effect is due to both the larger curvatures associated with smaller particle radii and the smaller total volumes for these systems. The densification rate is also strongly affected by configurational effects; the infinite line of cylinders, with two contacts per particle, reached its equilibrium configuration faster than two particles sharing a single contact.

Work is currently ongoing to extend the methodology employed here to consider axisymmetric configurations of spherical particles and compare model predictions to experimental results (Martínez-Herrera and Derby, 1993). Our technique is also potentially applicable to truly three-dimensional particles and configurations. The drawback of this approach is the difficulty encountered in describing topological changes of the particle geometry, such as the initial contact of particles and the subsequent formation of necks as well as the disappearance of a pore within a surrounding fluid matrix. However, existing analytical expressions for these limits (Frenkel, 1945; Mackenzie and Shuttleworth, 1949; Hopper, 1990, 1991) may well describe the asymptotic continuum behavior of these phenomena. Of course, the continuum equations themselves are not valid for the description of initial particle contact or final pore closure, where atomistic phenomena are important. However, unlike drop and bubble coalescence where approach and contact phenomena are quite important (see Davis, 1993), ceramic particles are generally pressed into a powder compact by the application of external forces and the initial formation of a small neck occurs very rapidly. Subsequent densification of particles is well described by continuum transport, so this approach will continue to be a useful tool to study many aspects of sintering phenomena.

Acknowledgments

This work was supported in part by the University of Minnesota Army High Performance Computing Research Center (under the auspices of Army Research Office contract number DAAL03-89-C-0038), the Minnesota Supercomputer Institute, the McKnight Foundation through a McKnight-Land Grant Professorship, and the National Science Foundation through a Presidential Young Investigator Award.

Literature Cited

Batchelor, G. K., *An Introduction to Fluid Dynamics*, Cambridge University Press, Cambridge (1967).

Benjamin, D. F., and L. E. Scriven et al., "Coating Flows: Form and Function," *Ind. Coating Res.*, **1**, 1 (1991).

Bird, R. B., W. E. Stewart, and E. L. Lightfoot, *Transport Phenomena*, Wiley, New York (1960).

Bolz, R. E., and G. L. Tuve, *CRC Handbook of Tables for Applied Engineering Science*, 2nd ed., CRC Press, Boca Raton, FL, Table 10.51B (1973).

Brinker, C. J., and G. W. Scherer, *Sol-Gel Science*, Academic Press, San Diego, CA, p. 675 (1990).

Brown, R. A., "Theory of Transport Processes in Single Crystal Growth from the Melt," *AIChE J.*, **34**, 881 (1988).

Cosgrove, G. J., J. A. J. Strozier, and L. L. Seigle, "An Approximate Analytical Model for the Late-Stage Sintering of an Array of Rods by Viscous Flow," *J. Appl. Phys.*, **47**(4), 1258 (1976).

Crank, J., *Free and Moving Boundary Problems*, Clarendon Press, Oxford (1984).

Crochet, M. J., "Numerical Simulation of Flow Processes," *Chem. Eng. Sci.*, **42**(5), 979 (1987).

Cuvelier, C., and J. M. Driessen, "Thermocapillary Free Boundaries in Crystal Growth," *J. Fluid Mech.*, **169**, 1 (1986).

Davis, R. H., "Microhydrodynamics of Particulate Suspensions," *Adv. Colloid Interf. Sci.*, **43**, 17 (1993).

Derby, J. J., "An Overview of Convection During the Growth of Single Crystals from the Melt," *Proc. of the Eighth International Summer School on Crystal Growth*, ISSCG-8, L. Boatner, ed., Palm Springs, CA (Aug. 9-15, 1992).
Derby, J. J., L. J. Atherton, P. D. Thomas, and R. A. Brown, "Finite Element Methods for Analysis of the Dynamics and Control of Czochralski Crystal Growth," *J. Sci. Comp.*, **2**, 297 (1987).
Derby, J. J., R. A. Brown, F. T. Geyling, A. S. Jordan, and G. A. Nikolakopoulou, "Finite Element Analysis of a Thermal-Capillary Model for Liquid Encapsulated Czochralski Growth," *J. Electrochem. Soc.*, **132**(2), 470 (1985).
Dhatt, G., and G. Touzot, *The Finite Element Method Displayed*, Wiley, New York (1984).
Engelman, M. S., R. L. Sani, P. M. Gresho, and M. Bercovier, "Consistent vs. Reduced Integration Penalty Methods for Incompressible Media Using Several Old and New Elements," *Int. J. Num. Meth. Fluids*, **2**, 25 (1982).
Evans, A. G., "Inhomogeneous Sintering: Stresses, Distortion and Damage," Defect Properties and Processing of High-Technology Nonmetallic Materials, Y. Chen, W. D. Kingery, and R. J. Stokes, eds., *Materials Res. Soc. Symposia Proc.*, Vol. 60, Mat. Res. Soc., Pittsburgh, 63 (1986).
Exner, H. E., "Principles of Single Phase Sintering," *Rev. Powder Metall. and Phys. Ceram.*, **1**(1-4), 7 (1979).
Frenkel, J., "Viscous Flow of Crystalline Bodies under the Action of Surface Tension," *J. Phys.*, **IX**(5), 385 (1945).
Glicksman, M. E., S. R. Coriell, and G. B. McFadden, "Interactions of Flows with the Crystal-Melt Interface," *Ann. Rev. Fluid Mech.*, **18**, 307 (1986).
Gresho, P. M., "Contribution to von Karman Institute Lecture Series on Computational Fluid Dynamics: Advection-Diffusion and Navier-Stokes Equations," Report UCRL-92275, Lawrence Livermore National Laboratory, Livermore, CA (1985).
Gresho, P. M., R. L. Lee, and R. L. Sani, "On the Time-Dependent Solution of the Incompressible Navier-Stokes Equations in Two- and Three Dimensions," *Recent Advances in Numerical Methods in Fluids*, Vol. 1, C. Taylor and K. Morgan, eds., Pineridge Press Ltd., Swansea, UK, p. 27 (1980).
Harmer, M. P., H. M. Chan, and D. M. Smyth, "Compositional Control of Ceramic Microstructures: An Overview," *Defect Properties and Processing of High-Technology Nonmetallic Materials*, Y. Chen, W. D. Kingery, and R. J. Stokes, eds., *Mat. Res. Soc. Symp. Proc.*, Vol. 60, Mat. Res. Soc., Pittsburgh, p. 125 (1986).
Hopper, R. W., "Coalescence of Two Equal Cylinders: Exact Results for Creeping Viscous Plane Flow Driven by Capillarity," *J. Am. Ceram. Soc. (Comm.)*, **67**, C262 (1984).
Hopper, R. W., "Plane Stokes Flow Driven by Capillarity on a Free Surface," *J. Fluid Mech.*, **213**, 349 (1990).
Hopper, R. W., "Plane Stokes Flow Driven by Capillarity on a Free Surface: 2. Further Developments," *J. Fluid Mech.*, **230**, 355 (1991).
Jagota, A., and P. R. Dawson, "Micromechanical Modeling of Powder Compacts: I. Unit Problems for Sintering and Traction Induced Deformation," *Acta Met.*, **36**(9), 2551 (1988).
Jagota, A., and P. R. Dawson, "Simulation of the Viscous Sintering of Two Particles," *J. Am. Ceram. Soc.*, **73**(1), 173 (1990).
Kheshgi, H. S., and L. E. Scriven, "Penalty Finite Element Analysis of Time-Dependent Two-Dimensional Free-Surface Film Flow," *Finite Element Methods in Fluids*, Vol. 5, J. T. Oden, ed., Wiley, New York (1983).
Kingery, W. D., H. K. Bowen, and D. R. Uhlmann, *Introduction to Ceramics*, 2nd ed., Wiley, New York, p. 448 (1976).
Kistler, S. F., and L. E. Scriven, "Coating Flow Theory by Finite Element and Asymptotic Analysis of the Navier-Stokes System," *Int. J. Num. Meth. Fluids*, **4**, 207 (1984).
Kuczynski, G. C., "Physics and Chemistry of Sintering," *Adv. Colloid Interf. Sci.*, **3**, 275 (1972).
Kuiken, H. K., "Viscous Sintering: the Surface-Tension-Driven Flow of a Liquid Form Under the Influence of Curvature Gradients at its Surface," *J. Fluid Mech.*, **214**, 503 (1990).
Levich, V. G., *Physicochemical Hydrodynamics*, Prentice-Hall, Englewood Cliffs, NJ (1962).
Mackenzie, J. K., and R. Shuttleworth, "A Phenomenological Theory of Sintering," *Proc. Phys. Soc.*, **62**(12-B), 833 (1949).
Martínez-Herrera, J. I., "Finite Element Analysis of the Sintering of Ceramic Powders," PhD Thesis, Dept. of Chemical Engineering and Materials Science, Univ. of Minnesota, Minneapolis (1994).
Martínez-Herrera, J. I., and J. J. Derby, "Viscous Sintering of Spherical Particles via Finite Element Analysis," *J. Am. Ceram. Soc.*, submitted (1993).
Mavridis, H., A. N. Hrymak, and J. Vlachopoulos, "Transient Free-Surface Flows in Injection Mold Filling," *AIChE J.*, **34**(3), 403 (1988).
Petzold, L., "Differential/Algebraic Equations are not ODE's," *SIAM J. Sci. Stat. Comput.*, **3**, 367 (1982).
Rabinovich, E. M., "Preparation of Glass by Sintering," *J. Mater. Sci.*, **20**, 4259 (1985).
Ross, J. W., W. A. Miller, and G. C. Weatherly, "Dynamic Computer Simulation of Viscous Flow Sintering Kinetics," *J. Appl. Phys.*, **52**(6), 3884 (1981).
Ruschak, K. J., "A Method for Incorporating Free Boundaries with Surface Tension in Finite Element Fluid-Flow Simulators," *Int. J. Num. Meth. Eng.*, **15**, 639 (1980).
Ruschak, K. J., "Coating Flows," *Ann. Rev. Fluid Mech.*, **17**, 65 (1985).
Scherer, G. W., "Sintering of Low-Density Glasses: I. Theory," *J. Am. Ceram. Soc.*, **60**(5-6), 236 (1977).
Scherer, G. W., "Viscous Sintering of a Bimodal Pore Size Distribution," *J. Am. Ceram. Soc.*, **67**(11), 709 (1984).
Shaw, N. J., "Densification and Coarsening During Solid State Sintering of Ceramics: A Review of Models: I. Densification," *Powder Met. Int.*, **21**(3), 16 (1989a).
Shaw, N. J., "Densification and Coarsening During Solid State Sintering of Ceramics: A Review of Models: II. Grain Growth," *Powder Met. Int.*, **21**(5), 31 (1989b).
Shaw, N. J., "Densification and Coarsening During Solid State Sintering of Ceramics: A Review of Models: III. Coarsening," *Powder Met. Int.*, **21**(6), 25 (1989c).
Shen, S.-F., "Simulation of Polymeric Flows in the Injection Moulding Process," *Int. J. Numer. Meth. Fluids*, **4**, 171 (1984).
Strang, G., and G. J. Fix, *An Analysis of the Finite Element Method*, Prentice-Hall, Englewood Cliffs, NJ (1973).
Szekely, J., "The Mathematical Modeling Revolution in Extractive Metallurgy," *Met. Trans. B*, **19B**, 525 (1988).
Thümmler, F., and W. Thomma, "The Sintering Process," *Metall. Rev.*, **12**, 69 (1967).
Ungar, L. H., N. Ramprasad, and R. A. Brown, "Finite Element Methods for Unsteady Solidification Problems Arising in Prediction of Morphological Structure," *J. Sci. Comp.*, **3**, 77 (1988).
van de Vorst, G. A. L., R. M. M. Mattheij, and H. K. Kuiken, "A Boundary Element Solution for Two-Dimensional Viscous Sintering," *J. Comp. Phys.*, **100**, 50 (1992).
Viskanta, R., "Heat Transfer During Melting and Solidification of Metals," *J. Heat Trans.*, **110**, 1205 (1988).
Voller, V. R., "An Overview of the Modelling of Heat and Fluid Flow in Solidification Systems," in *Modeling of Casting, Welding, and Advanced Solidification Processes V*, M. Rappaz, M. R. Ozgu, and K. W. Mehin, eds., The Metallurgical Society, Warrendale, PA, p. 661 (1991).
Waldron, M. B., and B. L. Daniell, *Sintering*, Heyden & Sons, London (1978).
Yan, M. F., "Sintering of Ceramics and Metals," in *Advances in Powder Technology*, G. Y. Chin, ed., American Society for Metals, Metals Park, OH, p. 99 (1982).

Manuscript received Sept 2, 1993, and revision received Dec. 10, 1993.